Dendrochronologia 69 (2021) 125877

Contents lists available at ScienceDirect

Dendrochronologia

journal homepage: www.elsevier.com/locate/dendro

ORIGINAL ARTICLE

Automated 3D tree-ring detection and measurement from X-ray computed tomography

Jorge Martinez-Garcia [a,*], Ingrid Stelzner [b], Joerg Stelzner [b], Damian Gwerder [a], Philipp Schuetz [a]

[a] Lucerne University of Applied Sciences and Arts, School of Engineering and Architecture, Horw, Switzerland
[b] Römisch Germanisches Zentralmuseum Mainz, Germany

ARTICLE INFO

Keywords:
Ring recognition
Edge detection
X-ray computed tomography
Dendrochronology

ABSTRACT

Tree ring analysis is essential to reveal the environmental information encoded in the wood structure. It provides quantitative data on the anatomical structure which can be used, for example, to measure the impact of the fluctuating environment on the tree growth, to support global vegetation models and for the dendrochronological analysis of archaeological wooden artefacts. Currently, several imaging-based methods for tree-ring detection and tree-ring feature estimation exist. However, despite advances in computer vision and edge recognition algorithms, detection of tree-rings is mostly limited to two-dimensional (2D) datasets and performed manually in some cases. This paper describes a new approach to estimate the three-dimensional (3D) structure of tree rings and their width automatically from X-ray computed tomography data. This approach relies on a modified Canny edge detection algorithm, which is capable of detecting fully connected tree-ring edges throughout the image stack. Our results show that this approach performs well on six tree species having conifer, ring-porous and diffuse-porous ring boundary structures. In our study, image denoising proved to be a critical step to achieve accurate results. A major advantage of this procedure is that it requires very little to no user interaction rendering it a reproducible procedure for tree-ring width measurements. As it also provides 3D representations of the ring edges, it also may be used in the future for the inspection of anatomical features.

1. Introduction

Tree rings formation is triggered by a succession of favourable and unfavourable growing conditions, governed by tree genetics and seasonality in photoperiod, temperature, and precipitation (Schweingruber, 1996; Fritts, 2001; Rathgeber et al., 2016). They are expressed as regions of contrasting tissues exhibiting a broad variability of anatomical structures depending on the species type and the environment (Schweingruber, 2007; Tarelkin et al., 2016). In temperate regions tree rings are generally composed of two anatomically distinguishable regions – the early- and latewood, separated by an abrupt or gradual density transition, i.e. the tree-ring boundary, however at lower latitudes the scenario is much more complex. Driven mostly by water availability and a weak seasonality in temperature, more than two regions can occur within annual rings of tropical species, which are hardly distinguishable in many cases (Silva et al., 2019; Abdul Azimin and Okada, 2014). Tree-ring boundaries can be distinct throughout the entire stem or part of it, and can be wedging or interrupted or simply indistinct, thus making the tree-ring analysis particularly challenging (Worbes, 2002; Worbes and Fichtler, 2010; Blagitz et al., 2019).

Quantitative analysis of tree-rings is crucial in the understanding, modelling and assessment of the evolution of the wood sample over time. To reveal the environmental information encoded in tree-rings, multiple quantitative parameters are generally required (Fonti et al., 2010; Anchukaitis et al., 2013; Zhang, 2015; García-González et al., 2016). Among them, tree-ring width (TRW) (i.e. distance between two consecutive tree-ring boundaries), for example, is a powerful and reliable proxy of environmental variability and in particular, climate fluctuations at various geographical and temporal scales (Dietz and Von Arx, 2005; Jones et al., 2009; Vannoppen et al., 2018). TRW has been used to investigate impacts of rising atmospheric CO_2 concentrations (Gedalof and Berg, 2010). In dendrochronology, TRW series are also commonly used to date the harvesting time of archaeological wooden samples and to perform growth release analyses, allowing the detection of historical

* Corresponding author.
E-mail address: jorge.martinezgarcia@hslu.ch (J. Martinez-Garcia).

https://doi.org/10.1016/j.dendro.2021.125877
Received 25 October 2020; Received in revised form 13 July 2021; Accepted 10 August 2021
Available online 20 August 2021

forest disturbance events (Čufar et al., 2015; Maes et al., 2017). Variation in TRW are also correlated to the intra-ring wood density profiles, which are indicators of wood quality and used to estimate the mechanical properties of the wood (Kharrat et al., 2019).

Tree-rings have been traditionally studied on stem cross sections (usually taken at breast height) and measured manually one-by-one by experts using appropriated equipment (e.g. with LinTab or Velmex systems), which is quite cumbersome and time-consuming (Speer, 2010). Alternative methods commonly use standard digital images of the specimen surface taken by digital cameras or scans, and image-processing based algorithms for tree-ring boundaries recognition. Conner et al. (1998) proposed a semi-automated tree ring dating system where rings are detected by a modified Canny algorithm. Laggoune et al. (2005) described a parametric tree-ring detection approach that is able to handle noisy edges in optical images, however, its results strongly depend on the kind of edge model function assumed. Cerda et al. (2007) proposed a tree-ring detection technique, which combines a Canny algorithm with a generalized Hough Transform and was tested in optical images of a wooden disk. Entacher et al. (2007) presented an algorithm for automated annual ring profile generation from CT-images, which applies a Mexican hat operator as approximation of the Laplacian operator. Wang et al. (2010) provided a method based on mathematical morphology and a Priority First Search algorithm to track tree-ring boundaries from micro-images of wood. Sundari and Kumar (2014) proposed an image processing approach to quantify the density of tree rings based on Sobel filters as edge detector. Fabijańska et al. (2017) presented an approach to an automatic tree-ring detection based on image gradient computations, which performed almost flawlessly in the case of conifer wood.

Some of the above algorithms have been implemented in *R*-based packages (Hietz, 2011; Lara et al., 2015; Campelo et al., 2019). MtreeRing, for example, is a flexible package with graphical interface for TRWs measurements (Jingning et al., 2019). ROXAS (written in Visual Basic 6.0) is an image analysis tool widely used to quantify anatomical structures and to calculate TRWs (von Arx and Carrer, 2014). There also exist commercial softwares enabling TRW measurements (e.g. WinDENDRO™, LignoVision™ and CooRecorder), but they are not optimal for all purposes because the accuracy of the results depends on the resolution of the scanned image (Speer, 2010). More recently, a deep learning approach, which applies a convolutional neural network (CNN) algorithm for a fully automated tree-ring detection has been proposed (Fabijańska and Danek, 2018). Its capability was successfully tested on optical images of three different wood species having ring-porous anatomical structure. Such Deep learning approaches could be promising to effectively detect tree-ring boundaries in large datasets, as those generated by X-ray or neutron computed tomography techniques. Remarkably, these procedures are rarely applied to a complete stack of CT cross-sections to extract the 3D morphology of the tree ring edge.

Several studies, however, have provided evidence for significant TRW variability along the axial direction (i.e. along the stem), for example, in tropical Loblolly pine (*Pinus taeda L.*) (Yu et al., 2014; Tasissa and Burkhart, 1997), Douglas fir (*Pseudotsuga menziesii*) (Gartner et al., 2002), European beech (*Fagus sylvatica* L.) (Bouriaud et al., 2005a) and Norway spruce (*Picea abies* (L.) Karst.) (Bouriaud et al., 2005b). In the latter, the axial TRW variability has been correlated to a decrease in climate sensitivity at higher stem cross-sections (Bouriaud et al., 2015; van der Maaten-T and Bouriaud, 2015; Peters et al., 2020). Furthermore, the successful application of 2D image-based TRW measurements requires proper treatment of the sample surfaces to remove impurities and unevenness, and to increase the contrast between early and late wood, which becomes exceedingly difficult to do in case of coated surfaces (Sass and Eckstein, 1994). Therefore, robust TRW and potentially other anatomical features (Novak et al., 2011; Rigling et al., 2002) measurements should account for both radial and axial variability throughout - virtually – the whole 3D sample volume. An assessment of the 3D morphology of the tree ring edge helps to supersede these preparatory steps as well as to replace correction methods to account for sample surfaces that are not orthogonal to tree ring edges. In addition, the application of computed tomography enables a non-destructive measurement of the sample which helps to preserve the sample in its original state.

Expanding the tree-ring analysis to 3D imaging data is feasible by using X-ray Computed Tomography (XCT). XCT is a powerful and non-destructive imaging technique which allows the inspection of the entire 3D volume of a sample at different length scales (Carmignato et al., 2018). XCT has already been successfully applied in the field of dendrochronology (Okochi et al., 2007). Grabner et al. (2009), Bill et al. (2012) and Stelzner and Million (2015), for example, have reported on the limits of the measurability of year ring widths. 3D tree-ring analysis has been performed on tree cores of different species (Van den Bulcke et al., 2014; De Mil et al., 2016; Maes et al., 2017; Vannoppen et al., 2017, 2018), using a method which exploits the 3D nature of the XCT imaging data to correct both ring growth and grain angles, overcoming several of the shortcomings of classical 2D X-ray densitometry (Van den Bulcke et al., 2014). Van den Bulcke et al. (2019) have also recently shown how to handle large physical increment core sets by using automated multiscale scanning and reconstruction. However, despite recent advances in XCT instrumentation and 3D tree-ring analysis, a methodology to account for tree-ring profile variability within the whole sample volume is still lacking.

In this contribution, a novel automated approach to extract the whole 3D tree-ring structure and estimate average TRWs from 3D XCT data is proposed. The approach uses a modified Canny algorithm as the edge detector combined with appropriated filters to recognize tree-ring surfaces. The applicability of the approach is illustrated by automatically extracting the tree-ring surfaces from 3D XCT data from six different wood species, quantifying their corresponding TRWs and comparing the results with those obtained by manual measurements on single CT scans images.

2. Materials and methods

Commercial samples of six wood species namely, Douglas fir (*Pseudotsuga menziesii*), Spruce (*Picea abies*), Larch (*Larix decidua*), Hemlock (*Tsuga heterophylla*), Cherry tree (*Prunus avium*) and Ash (*Quercus robur*) from Lignum, Zurich, Switzerland, were used in this work to test the performance of the approach (Lignum, 2020). The samples of parallelepiped shape with dimensions ($3 \times 1 \times 3$) cm^3 were cut for each wood type.

The tomographic analysis was performed on the in-house a laboratory XCT system (Diondo d_2, Germany). The measurements were conducted by setting the X-ray source XWT-225 TCHE+ from X-ray works, Garbsen, Germany in high power mode and choosing an operation voltage of 80 kV and a filament current of 300 μA. The wood samples were stacked on top of each other, mounted in a sample holder and placed in the sample chamber. The sample was rotated 360° in continuous mode during the acquisition. The radiographical projections were recorded with an X-ray detector 4343 DX-I from Varex, Salt Lake City, U. S.A., with a pixel size of 139 μm. The distance between the X-ray source and the sample and between the X-ray source and the detector was 159 and 1100 mm respectively, giving a magnification of 6.92 and a nominal voxel size of 20 μm. A total of 2400 projections images were acquired during the sample rotation of 360°. The resulting projections were converted into a 3D image stack of $2400 \times 2400 \times 3000$ voxels using the CERA reconstruction software based on the filtered back projection Feldkamp algorithm (Feldkamp et al., 1984) from Siemens.

Image cross-sections and 3D renderings of the wood were visualized in VGStudioMax3.3© and ImageJ-2.0 (Rasband, 1997) software. All algorithms used in this contribution were implemented in Python 3.7, supported by tools provided by the open-source image processing libraries scikit-image and OpenCV in combination with the scientific data

visualization cross-platform library Mayavi 4.7.2.

3. The proposed approach

In this section, the image processing approach developed to detect and quantify TRWs using 3D XCT imaging data is described. The main goal of the approach is to accurately calculate 3D tree-ring coordinates along the whole ring profile for subsequent TRW computations. A pipeline overview of the approach is displayed in Fig. 1 and explained in the following sections. To facilitate the reproduction of this paper's results for the reader, the source code of the presented algorithms is available from the corresponding author upon request.

3.1. Image denoising

Noise in CT images may impede the extraction of microstructures from the cross-sectional images. This unwanted issue may arise from instrumental setups (e.g. scattered radiation), measurement protocols (e.g. source filtration, number of projections, detector noise), or postprocessing and reconstruction. Since the tree-ring detection mechanism is mainly based on gradient computations, the edge detection results are very sensitive to image noise. Therefore, image denoising at the beginning is a critical pre-processing step to increase the accuracy of the edge recognition output.

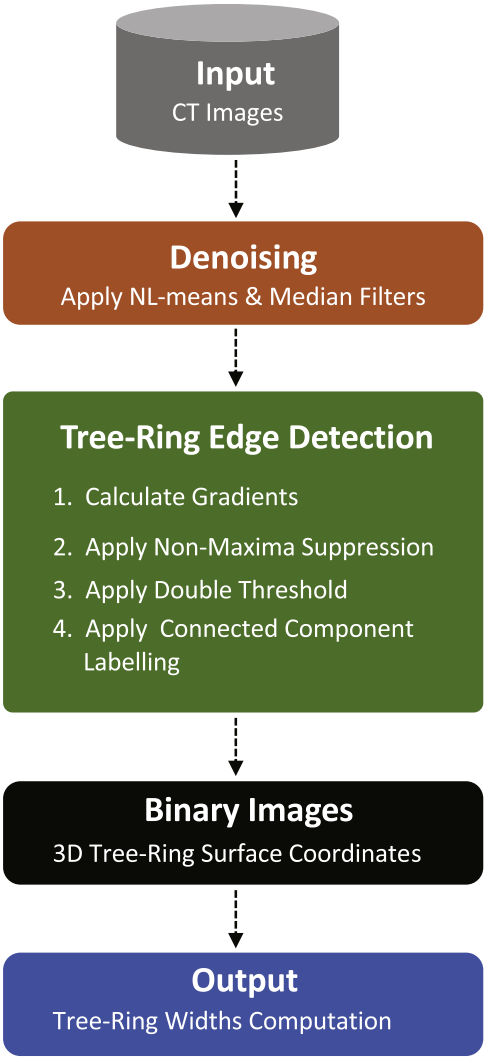

Fig. 1. (a) The pipeline overview of the proposed approach. The measured XCT image stack is firstly loaded as input data. Secondly, the 3D imaging data is filtered by combining the NL-means and median filters (Section 3.1). Then, the tree-ring edge detection algorithm is applied slice-by-slice to generate a new binary 3D image stack from which the tree-ring surface coordinates are calculated (Section 3.2). Finally, the corresponding TRWs are computed (Section 3.3).

Two non-linear smoothing filters which maintain the key tree-rings' features for subsequent edge detection have been applied in this work for image noise suppression, namely the non-local means (NL-means) and the median filters (Buades et al., 2011; Yang and Huang, 1981).

In the NL-means algorithm, the output value $\mathcal{I}_i$ at a given pixel, i, is computed as a weighted average of all N gray intensity values I_j in the image,

$$\mathcal{I}_i = \sum_j^N w_{ij} I_j, \quad w_{ij} = \frac{e^{-\frac{\|I(\mathcal{V}_i)-I(\mathcal{V}_j)\|_a^2}{h^2}}}{\sum_j e^{-\frac{\|I(\mathcal{V}_i)-I(\mathcal{V}_j)\|_a^2}{h^2}}}, \tag{1}$$

where the family of weights w_{ij} depends on the similarity between the pixels i and j. The larger weight contributions correspond to the pixels whose neighbourhoods, $\mathcal{V}_j$, are the most similar to the neighbourhood of the one to be denoised, $\mathcal{V}_i$. As a result, the NL-means algorithm can restore well texture, that would be blurred by other denoising algorithms. In a standard algorithm's implementations, the user has to set two parameters: the smoothing factor, h, which stands for the distance between similar neighbourhoods and the standard deviation, σ, which account for the image noise.

In contrast to NL-means, the median filter has a local character and does not use weights, but returns as an output, the median of the intensity values I_j compressed in a specified kernel neighbourhood $\mathcal{V}_i$ of the pixel i (e.g. a disk of radius r):

$$\mathcal{I}_i = \text{median}(I_j, j \in \mathcal{V}_i). \tag{2}$$

The combination of the algorithms implemented in the scikit-image Python package of both filters was found to be very effective in removing all unwanted image artefacts while maintaining the key features of the tree-rings edges. Both 3D and 2D versions of the filters can be equally applied at this stage.

3.2. Tree-ring edge detection

To calculate the tree-rings coordinates, it is required to firstly extract the line edges, which represent the tree-ring boundaries from the background. Since the ring boundaries are characterized by a sharp transition of intensity from latewood to earlywood, the magnitude of the image's gradient helps to detect it.

We propose here a modified version of the 2D Canny edge detector algorithm (Canny, 1986) which operates slice by slice in the volumetric 3D imaging data and incorporates some of the ideas discussed by Conner et al. (Conner et al., 1998), combined with the Otsu threshold, connected-component labeling (CCL) algorithm and the NL-means and median filters given in Eqs. (1) and (2).

3.2.1. Gradient computation

For each previously denoised XCT slice, $\mathcal{I}$, the horizontal and vertical Sobel operators are applied to determine the image gradient, $\nabla G = [\mathcal{I}_x, \mathcal{I}_y]$, whose magnitude $\mathcal{G}$ and orientation Θ at each pixel location are determined as:

$$\mathcal{G} = \sqrt{\mathcal{I}_x^2 + \mathcal{I}_y^2}, \tag{3}$$

$$\Theta = \arctan2(\mathcal{I}_y, \mathcal{I}_x), \tag{4}$$

where $\mathcal{I}_x$ and $\mathcal{I}_y$ are the image partial derivatives along the x and y axes. The output images $\mathcal{G}$ and Θ provide a strength edge map and the angles of the normal to the edges at each local point, respectively. Sobel filters implementations in Open CV and scikit-image Python's libraries are

suitable for this purpose.

3.2.2. Non-maximum suppression

To thin out the edges captured in $\mathcal{G}$, a non-maximum suppression algorithm (NMS) is developed, which reduces multiple edge responses by searching for local maxima in $\mathcal{G}$ as the most probable real tree-ring edges points. In contrast to the traditional Canny edge-detector, physical characteristics of tree-rings are here introduced to prevent false intra-ring edges detection and to reduce the algorithm's sensitivity to local pixel variations, as proposed in Conner et al. (1998). The algorithm is implemented as follows:

1. *Quantifying the gradient's directions*: The continuous gradient directions, Θ_{ij}, are rounded to the nearest multiple of 45° to conform to one of 8 discrete directions, $\Omega_n = \{n\frac{\pi}{4};\ n = 0,1,2,\ldots,7\}$, as shown in Fig. 2.
2. *Tracking tree-ring orientation*: The average gradient magnitude, for each of the eight discrete directions, $\langle \mathcal{G}_{ij} \rangle_n$, is computed. The direction Ω_m with the largest gradient average magnitude, corresponds to the orientation with the highest probability of being the tree-ring orientation in the region of interest:

$$\Omega_m \rightarrow \max\left\{\langle \mathcal{G}_{ij} \rangle_n;\ m \in [n]\right\} \tag{5}$$

3. *Selecting tree-ring edges*: The gradient magnitude at each local pixel, $\mathcal{G}_{ij}$, is compared with those of their two closest neighbouring pixels lying along the average tree-ring orientation, Ω_m. If $\mathcal{G}_{ij}$ is greater than those of the neighbours of interest and the grey level intensity $\mathcal{I}$ of the pixel neighbour located at Ω_m is greater than that of the neighbour located at $\Omega_m + \pi$, it is considered to be a local maxima and part of a true tree-ring edge. Therefore it will be preserved in the output image. Otherwise, it would be suppressed. It is here assumed that the pith of the wood is along $\Omega_m + \pi$ and the bark along Ω_m. For example, to the top and to the bottom, for horizontal tree-rings with normals along $\Omega_0 = 0°$, respectively.

3.2.3. Final edge tracking

The output edge map from the NMS algorithm contains 1 pixel-wide edge structures of variable intensities, corresponding to true tree-ring edges but also possibly to extraneous noise features (e.g. knots, resin ducts, etc.). To achieve an accurate result, the latter spurious responses are removed as follows:

1. *Double thresholding*: Two thresholds values, t_s and $t_i (t_s > t_i)$, are computed to classify all pixels in $\mathcal{G}$ into three different classes: Strong $(\mathcal{G} \geq t_s)$, weak $(t_i \leq \mathcal{G} < t_s)$ and non-relevant $(\mathcal{G} < t_i)$. Non-relevant pixels are set to zero (background) and the strong pixels are set to white (foreground) in the output image. Weak pixels are considered candidates for foreground or background, depending on their connectivity. The high threshold t_s is determined by using the Otsu's method (Otsu, 1979) as implemented in the scikit-image Python library, whereas the lower threshold is set to $0.5t_s$, for each cross-sectional image.
2. *Connected component analysis*: To finalize the edge detection, a kind of CCL algorithm (Wu et al., 2005) is developed to classify weak pixels into foreground or background. For each weak pixel candidate, its 8-connected neighbouring pixels are analysed. If at least one of the neighbours is strong, it becomes strong too and the current label is assigned to it. Otherwise it is classified as background. In the end, a binary output image with fully connected and uniquely labelled edges is obtained as foreground.

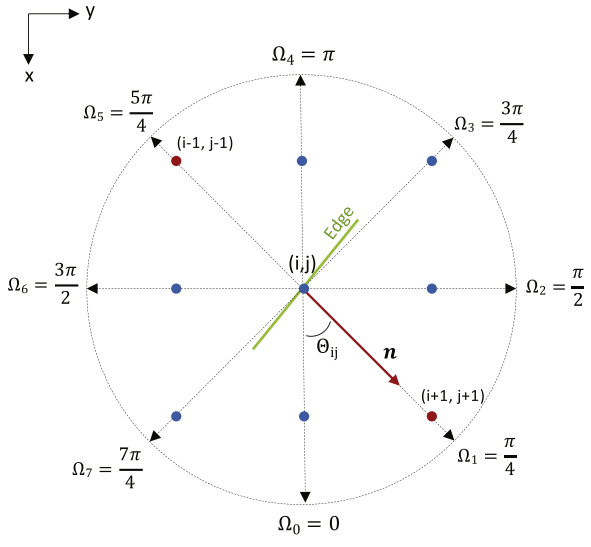

Fig. 2. Schematic overview of the elements in the NMS algorithm. The eight discrete directions, $\Omega_n = \left\{n\frac{\pi}{4};\ n = 0,1,2,\ldots,7\right\}$, are represented with black arrows in a neighbourhood of the current pixel (i, j). The overall tree-ring orientation (i.e. angle of the normal to edge, **n**, with respect to the x-axis) coincides with $\Omega_1 = \pi/4$. The two neighbouring pixels relevant to (i,j) in the algorithm are represented in red.

3.3. 3D tree-ring width calculations

Tree-ring widths are here calculated as the average distance between two consecutive tree-ring surfaces, which are determined from the 3D image data as follows.

1. *Determining tree-ring surfaces*: Given a 3D image stack, a Cartesian coordinate system is chosen such that the z-axis is parallel to the stacking direction and the mutually perpendicular x and y axes lie on the image plane, as shown in Fig. (3). The edge-detector algorithm proposed in Section (3.2) is then applied on each 2D CT slice, to generate a new binary 3D image stack having tree-ring surfaces in the foreground as output.
2. *3D tree-ring coordinates*: Running over all slices in the binary stack, the 3D tree-ring coordinates are calculated from the foreground and labelled as, $R_{j,i,w} = (x_j, y_j, z_w)_i$, where $R_{j,i,w}$ stands for the position vector of the jth point lying on the ith tree-ring at the slice w (see Fig. 3).
3. *Tree-ring width*: Starting with a pair of consecutive rings in the wth slice, the orientation θ of the vector pointing from the first point $R_{0,i,w}$ in the ith ring to the current j-ending point in the subsequent $(i + 1)$ ring, $R_{j,i+1,w}$, is calculated for all j. When the angle matches the orientation of the normal vector to the ith ring in a tolerance zone of

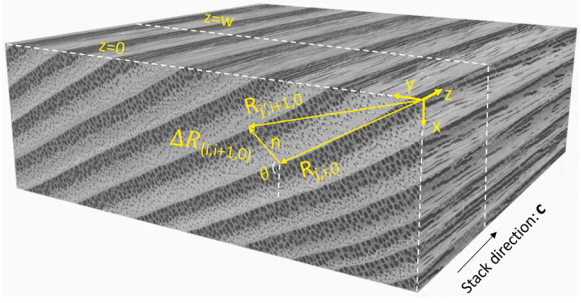

Fig. 3. A measured XCT image stack of Ash wood and its associate Cartesian coordinate system, $C\{x, y, z\}$. Two points, j and j', at two consecutive rings, i and $i + 1$, on the XCT slice, $z = 0$, are represented by their corresponding positional vectors, $R_{j,i,0}$ and $R_{j',i+1,0}$. The magnitude of the difference vector $\Delta R_{i,i+1,0}$ with orientation θ, and parallel to the structure direction **n**, is taken as the ring-width between the two points.

five degrees, the two points are used to evaluate the width as the Euclidean distance. By looping over all j-points in the ith ring, for all slices w, a set of pairwise distances are generated, whose average value, $d_{(i,i+1)} = \langle d_{ij,(i+1)j} \rangle_j$ is taken as a representative measure of the corresponding tree-ring width. The angle of the normal vector $\mathbf{n}$ to the current ring is here approximated by the overall tree ring orientation, Ω_m given in Eq. (5). The direction of $\mathbf{n}$ is assumed here to be defined in the XCT slices (see Fig. 3), a condition that is fulfilled in all the examples considered in this work. If the latter does not apply, the corresponding structure direction $\mathbf{g}$ should be determined first as proposed in Van den Bulcke et al. (2014). Then, the previously calculated $d_{(i,i+1)}$ metrics should be multiplied by the factor of $\cos(\psi) = \mathbf{n} \cdot \mathbf{g}$, where ψ is the angle between $\mathbf{n}$ and $\mathbf{g}$.

4. Results and discussion

The proposed approach described above, was applied to detect tree-rings and quantify TRWs in six samples of modern wood species with different anatomical structures, namely: ash, cherry, larch, hemlock, spruce and Douglas fir. The selection of the wood species is justified hereafter.

The obtained results are summarized in Fig. (4). In the left column, X-ray CT cross-sectional images of the six samples are shown, representing ring-porous wood (Fig. 4a), diffuse-porous wood (Fig. 4b) and conifer wood (Fig. 4c–f). As it can also be seen from Fig. (3), the ring-porous structure of ash mainly differ from the rest by the presence of large pores (i.e. vessels) in the earlywood, forming the rings. In contrast to the ash, the diffuse-porous structure of cherry (Fig. 4b), is characterized by pores of relatively small sizes distributed fairly evenly throughout the wood. All softwood samples (Fig. 4c-f), on the other hand, present a non-porous conifer like anatomical structure, consisting mainly of tracheid cells forming pairs of light and dark bands. All the XCT images were acquired with a spatial resolution of 20 μm, which was good enough to properly resolve the tree-rings boundaries of all wood species. The detected 2D tree-ring boundaries are marked in red.

The results of applying the numerical approach to each sample, are presented in the middle and right columns of Fig. (4). In the middle column, 3D plots of the extracted tree-ring positions for all XCT slices in the corresponding stack, i.e. the tree-ring surfaces, are displayed. As it can be seen from the plots, the tree-ring detection approach performs very well for all wood samples considered in this study. A putative reason for this excellent recognition is that for almost all cases, the tree-ring edges are well defined and fully connected. The key issue to achieve such highly accurate results, relies on providing properly denoised and edge enhanced input images to the edge detection algorithm. In order to accomplish this, the two nonlinear filters described in Section (3.1) were applied sequentially.

Table 1, reports the optimal combination of the filters' parameters used in this work for each wood sample species considered. As it can be seen, application of the NL-means filter with a standard deviation $\sigma = 15$–35 and smoothing factor, $h = 1.0$, followed by a median filter with a disk radius of, $r = 5$–11 pixels, were enough to provide accurate results for the examined samples. The optimal choice of the parameters, however, will depend on the complexity of the wood species, which in turn will determine the spatial resolution to be used in the XCT measurements. In general, the spatial resolution should be chosen high

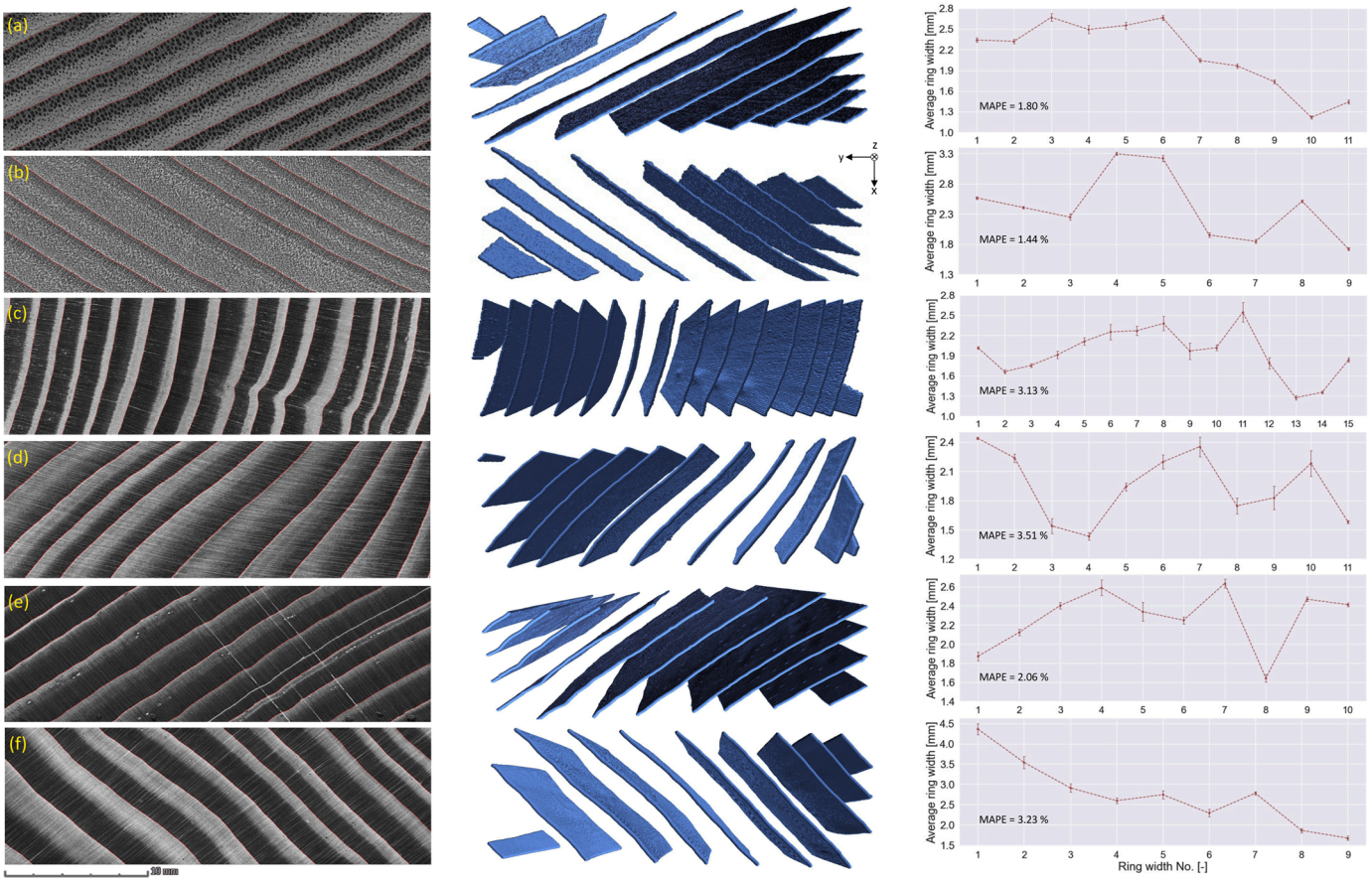

Fig. 4. Visualisation and analysis of tree ring properties. (left column) X-ray CT cross-sections of the 6 modern wood samples: (a) ash, (b) cherry tree, (c) larch, (d) hemlock, (e) spruce and (f) Douglas fir. (middle column) Visualisation of the extracted tree-ring positions. (right column) Average width of the tree rings calculated as average over the pairwise distances between two points of two consecutive tree rings. The length of the bars around the points corresponds to the magnitude of the standard deviation.

Table 1
Filter parameters values used in this work.

Wood species	NL-means filter		Median filter
	σ	h	r [pix]
Ash	30	1.0	11
Cherry tree	35	1.0	10
Larch	25	1.0	10
Hemlock	30	1.0	5
Spruce	15	1.0	9
Douglas fir	15	1.0	9

enough to fully resolve the tree-ring boundaries and at the same time, low enough to omit the presence of prominent anatomical features (e.g. wood-rays, pores, cells, etc.), which could act as noise and therefore complicate the subsequent denoising and tree-ring detection image-based procedures.

It should be stressed that repeated combinations of both filters, might lead to excessive enhancements of false tree-ring (i.e. intra ring earlywood-latewood boundaries) and other high contrast structures, which could complicate the subsequent true-edge recognition step. When such undesired high contrast features are orthogonally oriented to the ring edges, for example rays or inter-ring connections found in the spruce sample (Fig. 4e), the NMS algorithm (Section 3.2.2) is robust enough to remove them. Other edge-preserving filters (e.g. bilateral and anisotropic diffusion) could also be applied for this kind of work. However, we recommend their use as a substitute of the median filter and in combination with the NL-means filter for optimum results. In addition, filtering was the most time-consuming part of the procedure, taking around 15-30 min on a standard laptop computer (16 GB RAM, IntelCore i9 2.4 GHz CPU), depending on the parameter setting. Nevertheless, the filtration has to be performed only once. Afterwards, edge recognition and tree-ring width computations takes on average only a few minutes.

Another important factor which improved the precision and accuracy of the edge detection, was a self-adaptive selection of the two threshold values. By using the Otsu method, both high and low thresholds are automatically selected based on the specific images' properties (i.e. minimizing the overall maximum in the between-class variances). This improvement also enables the automatic application of the edge detection algorithm on a 3D image stack, where self-determined optimal threshold values are applied to each cross-sectional image. This is a substantial extension of the traditional Canny algorithm, where a simple Gaussian filter is adopted and both thresholds are defined empirically, which may cause excessive smoothing of the image, resulting in edges which are either fragmented or lost.

The computed averaged TRWs as a function of the number of consecutive ring pairs (i.e. average TRW profiles), are shown in the right column of Fig. 4. The total number of tree-rings observed in the cross-sectional XCT images of the wood samples vary from 10, present in Douglas fir and cherry, to 16 observed in Larch. TRW profiles were found to be different for different wood species, being the case of Douglas fir where the highest TRW variation among the rings, $\Delta\mathrm{TRW} = 2.7$ mm, was observed.

As it can be seen from the computed tree-ring surfaces, all tree-rings displayed a rather uniform shape along the z-direction, hence the TRW profiles at different height levels (i.e. z-values), were generally very close to those averages reported in the figure. This is confirmed by the small standard deviation values, σ_{TRW}, obtained for each measurement (see error bars in Fig. 4).

To assess the variability of the computed TRW profiles, the mean absolute percentage error metric (MAPE) was calculated for each wood samples as follows,

$$\mathrm{MAPE} = \frac{100}{n}\sum_{i}^{n}\frac{\sigma_{\mathrm{TRW}_i}}{\langle \mathrm{TRW}\rangle_i}, \tag{6}$$

where n is the total number of consecutive ring pairs (i.e. sample size) and σ_{TRW_i} is the standard deviation associated to average TRW of the ith rings pair, $\langle \mathrm{TRW}\rangle_i$.

The computed MAPE values for all wood samples were found to be less than 10%, where hemlock and Douglas fir had the highest values. The low MAPE values indicate a low tree-ring shape variability for all samples examined, which is an expected result as all detected tree-ring boundaries are fairly flat surfaces. A comparison with manual measurements is displayed in Table 2, which also reports the main output values from the automated approach. Manual TRW measurements were conducted for each wood species by measuring the distance between two points at adjacent rings along the ring growth direction using the ImageJ software as shown in Fig. (5)a. Fig. (5)b displays the automatically determined TRW value: for each calculated tree-ring coordinate, the pairwise distance to the neighbouring tree-ring edge is calculated along the normal vector to the tree-ring [see Fig. (3)]. The reported TRW is obtained by averaging over all pairwise distances computed along the whole profile of two consecutive rings throughout the 3D image stack.

The results indicate that manual and automatic TRW values match very well. The deviations are between −0.16 and 0.28 mm corresponding to a maximum deviation of 14 voxels. The highest accuracy was obtained for cherry, which had the lowest values for the RMSE, ME and VAR metrics. However, slight differences occur in some particular rings (e.g. TRW No. 4 in Spruce), which might have an impact on the attribution of the dating period. It is important to note that this difference also could be routed in the procedure of manual TRWs measurement as the results strongly depend on which two points are selected. An advantage of the proposed automated method is that it is not dependent on the user's experience and therefore it enables a reproducible dating process.

For samples exhibiting tree-rings with more complex structures and significant curvature, higher MAPE values and consequently, higher deviation from manually TRWs estimation should be expected. This point will be addressed in future research.

5. Conclusions

A new image processing approach was developed to extract 3D tree-rings and calculate tree-ring widths automatically from X-ray computed tomography data. A key advantage of this algorithm is that it can extract the tree ring edges automatically with little to no user interaction. Therefore, it is optimally suited to analyse many samples as well as analyse XCT image stacks. The approach is based on an improved Canny edge detection algorithm which incorporates the NL-means and median smoothing filters to suppress image noise and a self-adaptive determination of the two threshold values.

The approach was tested using 3D XCT tomography imaging data obtained from six modern wood samples having different anatomical structure. From the data, well defined 3D tree-ring surfaces and their corresponding Cartesian coordinates were extracted with the voxel grid precision. TRWs were computed using a new algorithm that calculates the TRWs, from averaged pairwise distances between two consecutive tree-rings. TRWs obtained from the automated method were found to agree perfectly well with TRW values measured manually for all samples examined. This significant agreement demonstrates the applicability of this approach. In addition, the procedures also automatically analyse the full 3D morphology of the ring edge. Therefore, cumbersome sample preparation (e.g. ensuring that the tree-ring edges are perpendicular to the cutting surface) or numerical correction procedures for non-perpendicularly cut samples are not required. These two advantages help to reduce sources of uncertainty and support less-experienced users in correct measurements of the TRWs. Furthermore, the possibility to automatically determine the 3D morphology of tree-ring edges may allow researchers to better understand the impact of anatomical features on tree-ring edges.

Table 2
Comparison of manual and automatic TRW measurements for each wood species. The degree of agreement is measured with the mean error (ME), the root mean square error (RMSE) and the variance, VAR = $RMSE^2 - ME^2$, metrics.

Wood species	TRW no.	TRW [mm] Manual	Automatic			Wood species	TRW no.	TRW [mm] Manual	Automatic		
			Avg.	Min.	Max.				Avg.	Min.	Max.
Ash	1	2.29	2.34	2.19	2.43	Hemlock	1	2.50	2.44	2.40	2.49
	2	2.20	2.32	2.20	2.47		2	2.34	2.24	2.13	2.35
	3	2.46	2.66	2.50	2.89		3	1.53	1.54	1.38	1.74
ME = 0.099	4	2.33	2.49	2.31	2.72	ME = −0.054	4	1.48	1.43	1.31	1.53
RMSE = 0.113	5	2.42	2.55	2.40	2.77	RMSE = 0.106	5	2.03	1.94	1.83	2.04
VAR = 0.003	6	2.58	2.66	2.54	2.79	VAR = 0.008	6	2.25	2.20	2.06	2.40
	7	1.95	2.04	1.92	2.16		7	2.49	2.35	2.14	2.57
	8	1.84	1.96	1.86	2.10		8	1.89	1.75	1.54	1.95
	9	1.71	1.73	1.59	1.85		9	2.01	1.83	1.57	2.11
	10	1.18	1.21	1.10	1.33		10	2.04	2.18	1.86	2.42
	11	1.39	1.44	1.35	1.57		11	1.51	1.58	1.55	1.63
	..	..		..			..	..		..	
Cherry tree	1	2.56	2.56	2.48	2.69	Spruce	1	1.90	1.87	1.75	2.00
	2	2.38	2.41	2.34	2.52		2	2.08	2.12	1.98	2.27
	3	2.23	2.25	2.12	2.42		3	2.34	2.40	2.29	2.55
ME = 0.014	4	3.24	3.29	3.19	3.39	ME = 0.047	4	2.35	2.59	2.31	2.76
RMSE = 0.031	5	3.20	3.22	3.05	3.42	RMSE = 0.106	5	2.50	2.34	2.12	2.59
VAR = 0.001	6	2.00	1.95	1.83	2.09	VAR = 0.009	6	2.18	2.25	2.11	2.41
	7	1.85	1.85	1.72	2.04		7	2.55	2.63	2.41	2.83
	8	2.48	2.51	2.43	2.63		8	1.63	1.64	1.53	1.75
	9	1.68	1.72	1.64	1.84		9	2.40	2.47	2.35	2.56
	..	..		..			10	2.33	2.41	2.32	2.49
Larch	1	1.98	2.01	1.94	2.14		..	..		..	
	2	1.66	1.66	1.56	1.76	Douglas fir	1	4.43	4.36	4.12	4.61
	3	1.80	1.75	1.66	1.84		2	3.70	3.54	3.30	3.96
ME = 0.028	4	1.94	1.91	1.76	2.02		3	2.78	2.91	2.68	3.14
RMSE = 0.10	5	2.08	2.11	1.96	2.22	ME = −0.014	4	2.64	2.59	2.43	2.77
VAR = 0.009	6	2.32	2.25	2.06	2.46	RMSE = 0.088	5	2.82	2.74	2.43	2.89
	7	2.17	2.27	2.12	2.44	VAR = 0.008	6	2.34	2.29	2.03	2.46
	8	2.19	2.38	2.06	2.54		7	2.77	2.77	2.65	2.91
	9	1.67	1.97	1.48	2.12		8	1.80	1.86	1.72	1.98
	10	1.99	2.02	1.78	2.24		9	1.58	1.66	1.55	1.78
	11	2.56	2.54	2.30	3.04						
	12	1.84	1.79	1.68	2.12						
	13	1.24	1.27	1.18	1.36						
	14	1.40	1.35	1.28	1.48						
	15	1.86	1.83	1.74	1.94						

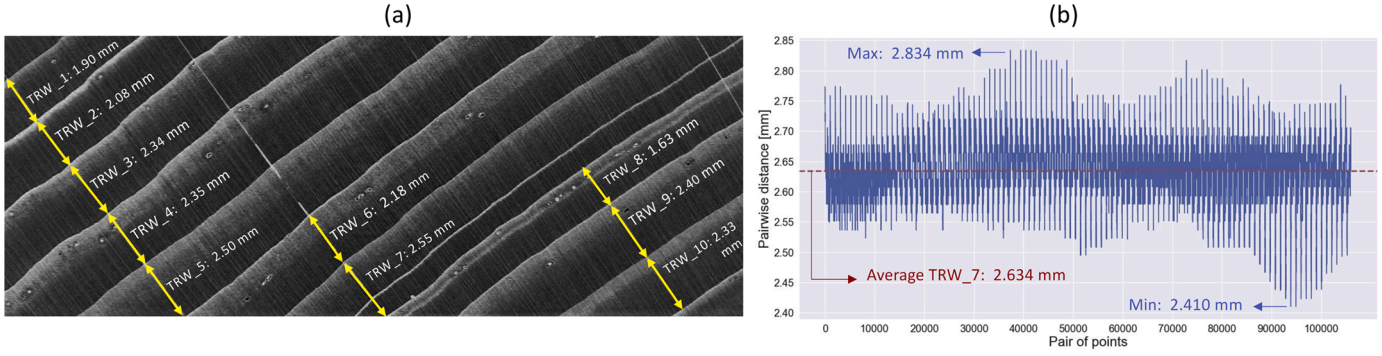

Fig. 5. TRW measurements in the spruce sample. (a) Manual measurement of all TRWs from a single CT slice. (b) Automatic measurement of the seventh TRW using the presented approach (Section 3.3).

Conflict of interest

None declared.

Declaration of Competing Interest

The authors report no declarations of interest.

Acknowledgements

The authors would like to thank to Dr. Oliver Nelle and Sebastian Million for fruitful discussions and suggestions and to Dr. Susan Braovac and Poppy O'Neill for reviewing the manuscript. This work was supported by the Swiss National Science Foundation (Grant 200021E 183684) and the German Research Foundation (DFG – 416877131).

References

Abdul Azimin, A.A., Okada, N., 2014. Occurrence and anatomical features of growth rings in tropical rainforest trees in peninsular Malaysia: a preliminary study. Tropics 23, 15–31.

Anchukaitis, Kevin, J.D., D'Arrigo, R., Andreu-Hayles, L., Frank, D., Verstege, A.A., Curtis, M., Buckley, B., Jacoby, G.C., Cook, E.R., 2013. Tree-ring-reconstructed summer temperatures from northwestern North America during the last nine centuries. J. Climate 26, 3001–3012.

Bill, J., Daly, A., Johnsen, Ø., Dalen, K.S., 2012. DendroCT – dendrochronology without damage. Dendrochronologia 30, 223–230.

Blagitz, M., Botosso, P.C., Longhi-Santos, T., Bianchini, E., 2019. Tree rings in tree species of a seasonal semi-deciduous forest in southern Brazil: wood anatomical markers, annual formation and radial growth dynamic. Dendrochronologia 55, 93–104.

Bouriaud, O., Brèda, N., Dupouey, J.-L., Granier, A., 2005b. Is ring width a reliable proxy for stem-biomass increment? A case study in European beech. Can. J. For. Res. 35, 2920–2933.

Bouriaud, O., Leban, J.-M., Bert, D., Deleuze, C., 2005a. Intra-annual variations in climate influence growth and wood density of Norway spruce. Tree Physiol. 25, 651–660.

Bouriaud, O., Teodosiu, M., Kirdyanov, A.V., Wirth, C., 2015. Influence of wood density in tree-ring-based annual productivity assessments and its errors in Norway spruce. Biogeosci. Discuss. 12, 5871–5905.

Buades, A., Coll, B., Morel, J.M., 2011. Non-local means denoising. Image Process. OnLine 1, 208–212.

Campelo, F., Mayer, K., Grabner, M., 2019. xRing–An R package to identify and measure tree-ring features using X-ray microdensity profiles. Dendrochronologia 53, 17–21.

Canny, J., 1986. A computational approach to edge detection. IEEE Trans. Pattern Anal. Mach. Intell. 8, 679–698.

Carmignato, S., Dewulf, W., Leach, R., 2018. Industrial X-Ray Computed Tomography. Springer, Cham.

Cerda, M., Hitschfeld-Kahler, N., Mery, D., 2007. Robust tree-ring detection. Pacific-Rim Symposium on Image and Video Technology 575–585.

Conner, W.S., Schowengerdt, R.A., Munro, M., Hughes, M.K., 1998. Design of a computer vision based tree ring dating system. IEEE Southwest Symposium on Image Analysis and Interpretation 256–261.

Čufar, K., Tegel, W., Merela, M., Kromer, B., Veluscek, A., 2015. Eneolithic pile dwellings south of the alps precisely dated with tree-ring chronologies from the north. Dendrochronologia 35, 91–98.

De Mil, T., Vannoppen, A., Beeckman, H., Van Acker, J., Van den Bulcke, J., 2016. A field-to-desktop toolchain for X-ray CT densitometry enables tree ring analysis. Ann. Bot. 117, 1187–1196.

Dietz, H., Von Arx, G., 2005. Climatic fluctuations causes large-scale synchronous variation in radial root increments of perennial forbs. Ecology 86, 327–333.

Entacher, K., Planitzer, D., Uhl, A., 2007. Towards an automated generation of tree ring profiles from CT-images. Proceedings of the 5th International Symposium on Image and Signal Processing and Analysis (ISPA 2007) 174–179.

Fabijańska, A., Danek, M., 2018. Deepdendro – a tree rings detector based on a deep convolutional neural network. Comput. Electron. Agric. 150, 353–363.

Fabijańska, A., Danek, M., Barniak, J., Piórkowski, A., 2017. Towards automatic tree rings detection in images of scanned wood samples. Comput. Electron. Agric. 140, 279–289.

Feldkamp, L.A., Davis, L.C., Kress, J.W., 1984. Practical cone-beam algorithm. J. Opt. Soc. Am. A 1, 612–619.

Fonti, P., von Arx, G., García-González, I., Eilmann, B., Sass-Klaassen, U., Gärtner, H., Eckstein, D., 2010. Studying global change through investigation of the plastic responses of xylem anatomy in tree rings. New Phytol. 185, 42–53.

Fritts, H.C., 2001. Tree Rings and Climate. Blackburn Press, Caldwell.

García-González, I., Souto-Herrero, M., Campelo, F., 2016. Ring-porosity and earlywood vessels: A review on extracting environmental information through time. IAWA J. 37, 295–314.

Gartner, B.L., North, E.M., Johnson, G.R., Singleton, R., 2002. Effects of live crown on vertical patterns of wood density and growth in Douglas-Fir. Can. J. For. Res. 32, 439–447.

Gedalof, Z., Berg, A.A., 2010. Tree ring evidence for limited direct CO_2 fertilization of forests over the 20th century. Glob. Biogeochem. Cycles 24, GB3027.

Grabner, M., Salaberger, D., Okochi, T., 2009. The need of high resolution μ-X-ray CT in dendrochronology and in wood identification. 2009 Proceedings of the 6th International Symposium on Image and Signal Processing and Analysis 349–352.

Hietz, P., 2011. A simple program to measure and analyse tree rings using Excel, R and SigmaScan. Dendrochronologia 29, 245–250.

Jingning, S., Wei, X., Qijin, L., Sher, S., 2019. Mtreering: an R package with graphical user interface for automatic measurement of tree ring widths using image processing techniques. Dendrochronologia 58, 125644.

Jones, P.D., Briffa, K.R., Osborn, T.J., Lough, J.M., van Ommen, T.D., Winther, B.M., Luterbacher, J., et al., 2009. High-resolution palaeoclimatology of the last millennium: a review of current status and future prospects. Holocene 19, 3–49.

Kharrat, W., Koubaa, A., Khlif, M., Bradai, C., 2019. Intra-ring wood density and dynamic modulus of elasticity profiles for black spruce and jack pine from X-ray densitometry and ultrasonic wave velocity measurement. Forest 10, 569.

Laggoune, H., Sarifuddin, Guesdon, V., 2005. Tree ring analysis. 'Canadian Conference on Electrical and Computer Engineering 1574–1577.

Lara, W., Bravo, F., Sierra, C.A., 2015. measuRing: an R package to measure tree-ring widths from scanned images. Dendrochronologia 34, 43–50.

Lignum, Holzwirtschaft Schweiz, 2020. www.lignum.ch.

Maes, S.L., Vannoppen, A., Altman, J., Van den Bulcke, J., Decocq, G., De Mil, T., Depauw, L., Landuyt, D., Perring, M.P., Van Acker, J., Vanhellemont, M., Verheyen, K., 2017. Evaluating the robustness of three ring-width measurement methods for growth release reconstruction. Dendrochronologia 46, 67–76.

Novak, K., de Luis, M., Cufar, K., Raventós, J., 2011. Frequency and variability of missing tree rings along the stems of *Pinus halepensis* and *Pinus pinea* from a semiarid site in SE Spain. J. Arid Environ. 75, 494–498.

Okochi, T., Hoshino, Y., Fujii, H., Mitsutani, T., 2007. Nondestructive tree-ring measurements for Japanese oak and Japanese beech using micro-focus X-ray computed tomography. Dendrochronologia 24, 155–164.

Otsu, N., 1979. A threshold selection method from gray-level histograms. IEEE Trans Syst. Man Cybern. 9, 62–66.

Peters, R.L., von Arx, G., Nievergelt, D., Ibrom, A., Stillhard, J., Trotsiuk, V., Mazurkiewicz, A., Babst, F., 2020. Axial changes in wood functional traits have limited net effects on stem biomass increment in European beech (*Fagus sylvatica*). Tree Physiol. 40, 498–510.

Rasband, W., 1997–2020. ImageJ. U. S. National Institutes of Health, Bethesda, Maryland, USA. . https://imagej.nih.gov/ij/.

Rathgeber, C.B.K., Cuny, H.E., Fonti, P., 2016. Biological basis of tree-ring formation: a crash course. Front. Plant Sci. 7 (734), 1–7.

Rigling, A., Bräker, O., Schneiter, G., Schweingruber, F., 2002. Intra-annual tree-ring parameters indicating differences in drought stress of *Pinus sylvestris* forests within the Erico-Pinion in the Valais (Switzerland). Plant Ecol. 163, 105–121.

Sass, U., Eckstein, D., 1994. Preparation of large thin sections and surfaces of wood for automatic image analysis. Holzforschung 48, 117–118.

Schweingruber, F.H., 1996. Tree Rings and Environment: Dendroecology. Paul Haupt AG, Bern.

Schweingruber, F.H., 2007. Wood Structure and Environment. Springer Berlin, Verlag.

Silva, Marcelo dos, S., Funch, Ligia, S., da Silva, Lazaro, B., 2019. The growth ring concept: seeking a broader and unambiguous approach covering tropical species. Biol. Rev. 94, 1161–1178.

Speer, J.H., 2010. Fundamentals of Tree-Ring Research. University of Arizona Press.

Stelzner, J., Million, S., 2015. X-ray computed tomography for anatomical and dendrochronological analysis of archaeological wood. J. Archaeol. Sci. 55, 188–196.

Sundari, P.M., Kumar, S.B.R., 2014. An approach for dendroclimatology using image processing techniques. In: 2014 World Congress on Computing and Communication Technologies (WCCCT). IEEE, pp. 234–236.

Tarelkin, Y., Delvaux, C., De Ridder, M., El Berkani, T., De Cannière, C., Beeckman, H., 2016. Growth-ring distinctness and boundary anatomy variability in tropical trees. IAWA J. 37, 275–294.

Tasissa, G., Burkhart, H.E., 1997. Modeling thinning effects on ring width distribution in loblolly pine (*Pinus taeda*). Can. J. For. Res. 27, 1291–1301.

Van den Bulcke, J., Boone, M.A., Dhaene, J., Van Loo, D., Van Hoorebeke, L., Boone, N. M., Wyffels, F., Beeckman, H., Van Acker, J., De Mil, T., 2019. Advanced X-ray CT scanning can boost tree ring research for earth system sciences. Ann. Bot. 124, 837–847.

Van den Bulcke, J., Wernersson, E.L.G., Dierick, M., Van Loo, D., Masschaele, B., Brabant, L., Boone, M.N., Van Hoorebeke, L., Haneca, K., Brun, A., Hendriks, C.L.L., Van Acker, J., 2014. 3D tree-ring analysis using helical X-ray tomography. Dendrochronologia 32, 39–46.

van der Maaten-T, M., Bouriaud, O., 2015. Climate-growth relationships at different stem heights in silver fir and Norway spruce. Can. J. For. Res. 42, 958–969.

Vannoppen, A., Boeckx, P., De Mil, T., Kint, V., Ponette, Q., Van den Bulcke, J., Verheyen, K., Muys, B., 2018. Climate driven trends in tree biomass increment show asynchronous dependence on tree-ring width and wood density variation. Dendrochronologia 48, 40–51.

Vannoppen, A., Maes, S., Kint, V., De Mil, T., Ponette, Q., Van Acker, J., Van den Bulcke, J., Verheyen, K., Muys, B., 2017. Using X-ray CT based tree-ring width data for tree growth trend analysis. Dendrochronologia 44, 66–75.

von Arx, G., Carrer, M., 2014. ROXAS – a new tool to build centuries-long tracheid-lumen chronologies in conifers. Dendrochronologia 32, 290–293.

Wang, H.-J., Qi, Heng-nian, Zhang, Guang-qun, Li, Wen-zhu, Wang, Bi-hui, 2010. An automatic method of tree-rings boundary detection on wood micro-images. 2010 International Conference on Computer Application and System Modeling. V2-477-V2-480.

Worbes, M., 2002. One hundred years of tree-ring research in the tropics – a brief history and an outlook to future challenges. Dendrochronologia 20, 217–231.

Worbes, M., Fichtler, E., 2010. Wood anatomy and tree-ring structure and their importance for tropical dendrochronology. Amazonian Flodplain Forests: Ecophysiology, Biodiversity and Sustainable Management. Springer, Berlin.

Wu, K., Otoo, E., Shoshami, A., 2005. Optimizing connected component labeling algorithms. Proc. SPIE – The International Society for Optical Engineering, Vol. 5747.

Yang, G.J., Huang, T.S., 1981. The effect of median filtering on edge location estimation. Comput. Graph. Image Process. 15, 224–245.

Yu, M., Cheng, X., He, Z., Wu, T., Yin, Z., 2014. Longitudinal variation of ring width, wood density and basal area increment in 26-year-old loblolly pine (*Pinus taeda*) trees. Tree-Ring Res. 70, 137–144.

Zhang, Z., 2015. Tree-rings, a key ecological indicator of environment and climate change. Ecol. Indic. 51, 107–116.